PNAS
www.pnas.org

Supplementary Information for

Evidence for a Northern Hemispheric trigger of the 100,000-year glacial cyclicity

Authors: Maayan Yehudai[1,2,3]*, Joohee Kim[1,2], Steven L. Goldstein[1,2]*, Leopoldo D. Pena[4], Maria Jaume-Seguí[1,4], Karla P. Knudson[1], Louise Bolge[1], Alberto Malinverno[1,2], and Torsten Bickert[5]

Affiliations:
[1] Lamont-Doherty Earth Observatory of Columbia University, USA
[2] Department of Earth and Environmental Sciences, Columbia University, USA
[3] Current address: Department of Climate Geochemistry, Max Planck Institute for Chemistry, Hahn Meitner-Weg 1, 55128 Mainz, Germany
[4] Department of Earth and Ocean Dynamics, University of Barcelona, Spain
[5] MARUM- Center for Marine Environmental Sciences, University of Bremen, Germany
*Correspondence to: my2430@columbia.edu; steveg@ldeo.columbia.edu

This PDF file includes:

1. Neodymium isotope ratios as tracers for Atlantic Ocean circulation

Nd isotope ratios in the oceans below surficial depths range from εNd <-20 in Baffin Bay to εNd ~0 in the Northwest Pacific (1, 2). NADW shows εNd ~-13 to -14, while North Pacific Deep Water (NPDW) has εNd of ~-2 to -4, with these differences reflecting Archean-to-Paleoproterozoic-aged continental-cratonic sources eroding into the North Atlantic, and inputs into the Pacific from mantle-derived volcanics around the Pacific rim. The values of the Circum-Antarctic and Indian Oceans are intermediate, with εNd between -7 to -9. The variability of Nd isotope ratios in the deep ocean today traces the global meridional overturning ocean circulation, with the Southern Ocean (εNd ~ -8) generally reflecting mixing between the NPDW (εNd ~ -4) and NADW (εNd ~ -13.5) end-members (e.g.: 1, 3, 4). Within the deep Atlantic, εNd-values have been described as 'quasi-conservative' (1), that is, showing the values expected from mixing of the northward flowing Southern Ocean water-masses and southward flowing North Atlantic Deep Water and thus strongly reflect the present-day structure of the AMOC (e.g.: 1, 3–6). Moreover, as a heavy element, the oceanic variability of Nd isotopic ratios reflects radioactive decay rather than mass dependent fractionation.

Past reconstruction of the AMOC is a challenging task because of the limitations associated with the different paleocirculation proxies (7–9). Nd-isotope ratios of authigenic phases in deep ocean sediment cores are unaffected by biological processes and in many cases have been shown to preserve the deep seawater Nd-signal (e.g.: 1, 2, 10–12), making them potentially useful for AMOC reconstruction. Since the AMOC's Atlantic and Pacific end-members sustain their distinctive present-day εNd-values through time (~-14 vs. ~-4, respectively, *Figs. 3, S3;* and refs. 6, 13), temporal changes at many locations between the end-members can be used to trace AMOC changes (1, 10–12, 14). However, since εNd-values in some locations have been shown to be sensitive to other potential factors such as local regional redox condition changes and sediment-seawater interactions (15–18), the choice of the core location is an important consideration to correctly reconstruct AMOC changes. In addition, a clear quantitative framework is not yet available for estimating the end-members mixing proportions or AMOC strength in the past; for example, the isotopic composition of a mixture depends on both concentrations and isotope ratios, and Nd concentrations in the end-members through time are poorly constrained. Also, the constancy of the εNd-values of the North Atlantic and North Pacific end-members indicated by the low temporal resolution Fe-Mn crust data *(Fig. S3)* obscures short-term variability. Therefore, *we currently use εNd as a qualitative measure of the impact/dominance of the Atlantic and Pacific end-members at any location, and as a reflection of the water-mass structure (rather than indicating paleo-water-mass fluxes)* along an ocean depth transect, reasonably assuming that the sites chosen mainly reflect the AMOC transport pathways (18).

This study is based on new data from two Atlantic Ocean deep drilling sites. North Atlantic DSDP Site 607 (41°00'N, 32°58'W, 3427 m) is on the western flank of the Mid-Atlantic Ridge , in the core of present day NADW (6, 19; *Fig. S1*). ODP Site 926 is located on the Ceara Rise in the equatorial Atlantic Ocean (3°43.1'N, 42°54.5'W, 3599 m; ref. 20), within NADW (*Fig. S1;* refs. 20, 21), close to the boundary between southward flowing NADW at shallower depths and northward flowing AABW at greater depths. Samples from Sites 607 and 926 were selected based on the published benthic $\delta^{18}O$ stratigraphy for the site (20, 22). The data (6, 21) are available from the EarthChem Data Library (https://ecl.earthchem.org/home.php), and are listed in *Tables S1 and S2*. Since Site 926 is not included in the global benthic LR04 stack (23) a new age model for it has been generated using tie points to LR04 as a reference, and interpolated in-between points *(Table S4)*. The tie points were produced based on glacial to interglacial transitions and glacial and interglacial maxima.

The new data in the North and Equatorial Atlantic are compared to sites from the South Atlantic (13, 24; *Fig. S1*). Southeast Atlantic ODP Site 1267 (28°5.88´S, 1°42.66´E, 4355 m) is in the Angola Basin, on the north side of the Walvis Ridge *(Fig. S1, Table S3,* ref. 24), currently bathed in NADW, and is partly modified by SSW. The southeast Atlantic (Cape Basin) ODP Sites 1088 (41°8.16'S, 13°33.77′E, 2082 m) and 1090 (42°54.82′S, 8°53.98'E, 3702 m), on the upper and lower boundaries of NADW, are those used by Pena and Goldstein (13) to identify the 'MPT-AMOC-disruption' between MIS-25-21 (950-850 ka). The chronologies of all the sites are based on comparison of benthic foraminiferal oxygen isotopes ($\delta^{18}O$) with the LR04 benthic stack (23).

Samples were chosen for Nd isotope analysis using the $\delta^{18}O$ record, targeting glacial and interglacial maxima of each core, in order to be able to compare the AMOC in different time-slices. Some data are presented between the maxima may not be coeval throughout the transect and therefore cannot be used in time-slices. However, at Site 607, transitional data are useful for elucidating the MIS-27-25 εNd-excursion *(Fig. S2)*. Published εNd-data are also presented from Site 1088 (25), and Site 929 (26) (6.0°N, 43.7°W, 4356 m), a deeper Site than 926 on the Ceara Rise.

2. Statistical analysis of the data prior to the 'MPT-AMOC-disruption'

In order to test whether the εNd-value of -15.8 in Site 607 during MIS-26 (between the MIS-26 glacial and the MIS-25 interglacial maxima) is anomalously negative with respect to the overall trend in the values leading up to it, a linear regression was conducted on the Site 607 data on glacial and interglacial maxima values for MISs 39-25 (*Fig. S7*). The lead-up trend was quantified as a linear trend $y = a + bx$, where the coefficients a and b were fitted by least-squares to the εNd-vs-age data while excluding the presumed anomalous MIS-26 value. To quantify the lead-up trend, a selected set of εNd-age pairs was used from the full data set in *Table S1.* The selected data for the glacial maxima values (MISs 38, 36, 34, 32, 30, 28, 26) and for the interglacial maxima values (MISs 39, 37, 35, 33, 31, 29, 27) were chosen based on the time window divisions in Figure 1 (pre-, during, and post-AMOC-disruption). Figure S7 also shows the confidence bands for each regression (that quantify the uncertainty of the fitted line for a given probability or p-value) and the prediction bands (that bracket the interval of predicted data from the line fit for a given p-value). The confidence bands were computed from standard least-squares using the sample variance of the misfit between the fitted line and the observed data. The prediction bands were computed using a Student's t distribution, which is a conservative choice that accounts for the additional uncertainty due to the use of sample statistics for the predicted values and their variance. All data analysis results are detailed in *Table S5*.

When taken together, the glacial maxima values for Site 607 display a well-defined trend toward increasingly negative εNd-values between MIS-38 and MIS-26 (*Fig. S7A)*, whereas the interglacial values do not show a noticeable trend (*Fig. S7D)*. To test whether the MIS-38 or MIS-26 values exert a large influence on the negative trend in the glacial εNd-values, we carried out the same analysis excluding each of these points (*Fig. S7B,C*). In an additional scenario, we excluded both MIS-38 and MIS-26 (*Fig. S7D*). When taking out each point separately (*Fig. S7B,C)*, the trend and the uncertainty bounds remain quite similar to the ones observed using all the glacial maxima (*Fig. S7A)*. However, when both MIS-38 and MIS-26 data points are omitted from the regression (*Fig. S7D)* the trend no longer holds, which implies that it is not statistically significant excluding those two points. Note that there is a limited amount of Nd-isotope data around the glacial maxima, and that there are only five glacial cycles included in this interval. Nevertheless, the *p*-value for the 'anomalous' MIS-26-star data point in this case is < 0.05, as it still falls outside of the 95% prediction band for both glacial and interglacial data at Site 607. This means that the εNd-value measured for this point is unlikely to be consistent with either the glacial or the interglacial trends, excluding any combination of points, supporting the notion that this εNd-value represents an unusual event.

The linear regression analyses of Site 926 data provide additional insight into the differences in the εNd patterns between the North Atlantic and the rest of the basin during the pre-MPT-AMOC-disruption period *(Figs. S7F,G,H,I)*. Site 926 glacial values yield a shallower slope *(Fig. S7F)* than that observed for Site 607 *(Fig. S7A)*. The weaker glacial trend at Site 926 versus the stronger one shown by Site 607 indicates that the strong pattern seen at the North Atlantic site is unique to that location. When omitting MIS-38 or MIS-26 glacial data points *(Fig. S7G,H,I)*, the slope of the Site 926 regression is much shallower, and the nominal slope value and uncertainty bounds point to the possibility of a 'negative' slope *(Fig. S7E)*. This is not the case for Site 607, where even when taking the uncertainty bounds into account, the slope prediction remains positive *(Fig. S7B,C),* except when both MIS-38 and MIS-26 are excluded *(Fig. S7D,I)*. Although there is clearly a difference in the glacial patterns observed at Sites 607 and 926, more data is required to determine whether the trend observed at Site 607 is significant or is driven by the more extreme values of MIS-38 and MIS-26. The interglacial pattern at Site 926 *(Fig. S7J)* is more variable than at Site 607 *(Fig. S7C),* which expands the interglacial uncertainty bounds and again emphasizes the relative stability of the North Atlantic εNd-values during interglacial maxima at Site 607.

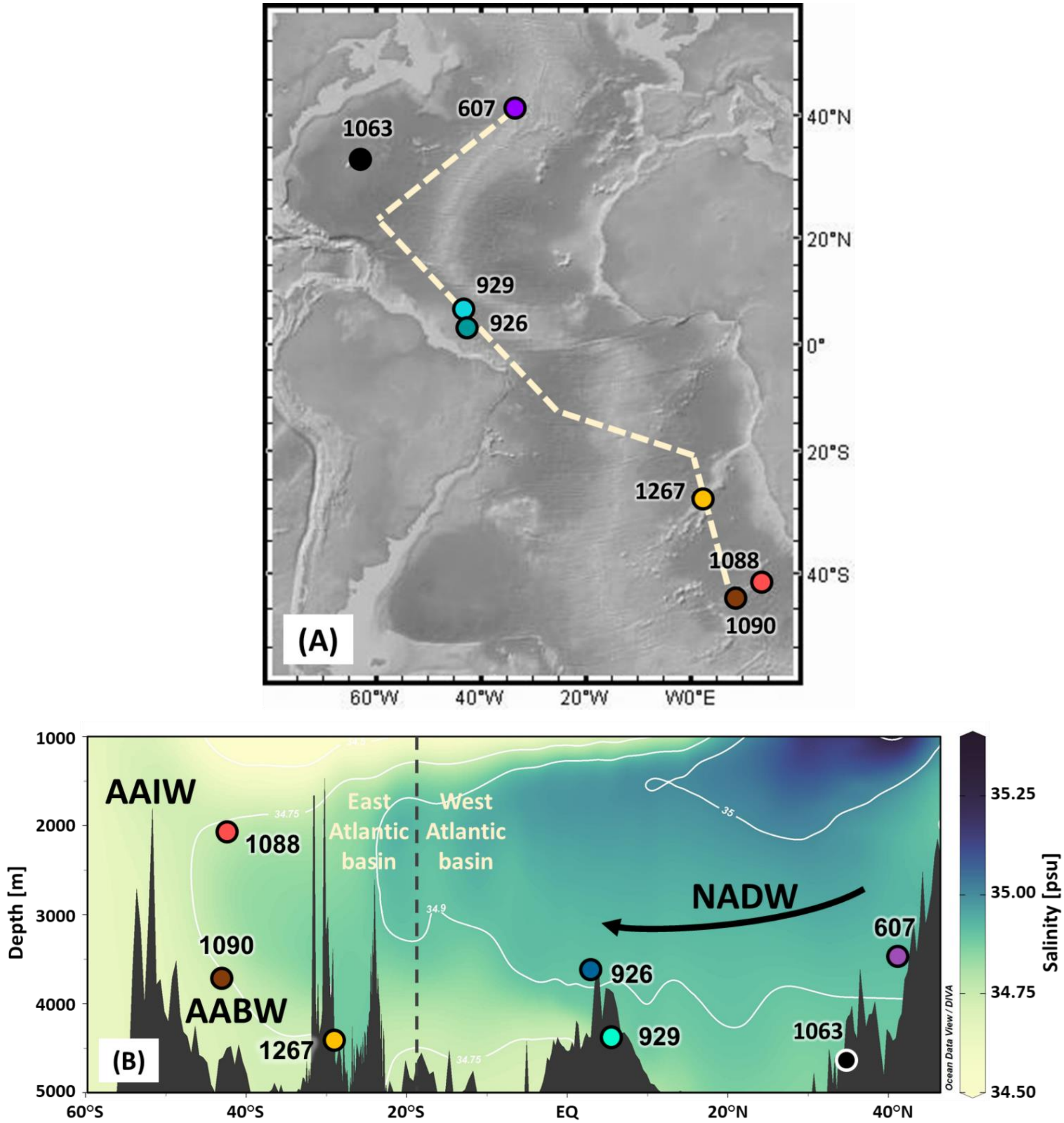

Figure S1. ***Core locations and present-day water mass distribution.*** (A) Map of the Atlantic Ocean, showing the sediment core sites discussed in the study. The dashed line represents the cross section in panel B. (B) A N-S salinity profile of the Atlantic Ocean showing the water masses. The transition from the western to the eastern basin is shown by the dashed line.

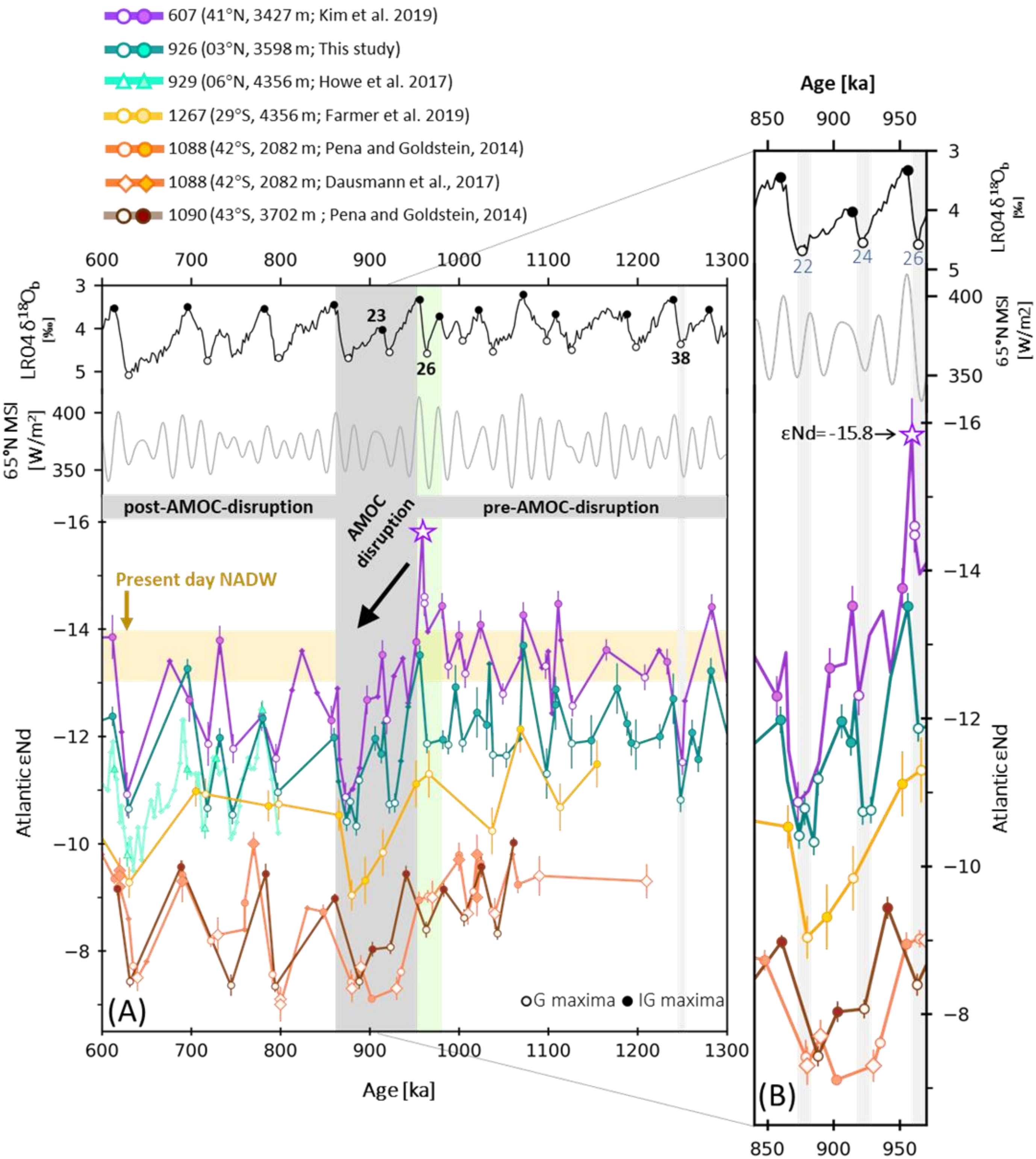
607 (41°N, 3427 m; Kim et al. 2019)
926 (03°N, 3598 m; This study)
929 (06°N, 4356 m; Howe et al. 2017)
1267 (29°S, 4356 m; Farmer et al. 2019)
1088 (42°S, 2082 m; Pena and Goldstein, 2014)
1088 (42°S, 2082 m; Dausmann et al., 2017)
1090 (43°S, 3702 m ; Pena and Goldstein, 2014)
LR04 δ18Ob [‰]
65°N MSI [W/m2]
post-AMOC-disruption
AMOC disruption
pre-AMOC-disruption
Present day NADW
Atlantic εNd
G maxima
IG maxima
(A)
Age [ka]
εNd=-15.8
(B)

Figure S2*. A north to south transect of the Atlantic Ocean εNd, reflecting AMOC changes through the MPT.* The time series is divided into three time-windows: ‘pre-AMOC-disruption’ refers to MIS-39-25 (~ 1280-950 ka), ‘MPT-AMOC-disruption’ to MIS-25-21 (~ 950-860 ka), and ‘post-AMOC-disruption’ to MIS-21-15 (~860-600 ka). Open circles are glacial maxima and solid circles are interglacial maxima, the open star is a highly negative intermediate point (between glacial and interglacial maxima) during MIS-26. All the records show glacial-interglacial zig-zags with glacials showing more positive εNd-values than interglacials. At each point in time, the more southerly records show stronger SSW εNd signals, and the MPT-AMOC-disruption impacts all the records. Together, this means the records reflect the AMOC. (A) LR04 benthic δ18O stack (top; 23), summer insolation at 65°N (gray) and new εNd data from Sites 607 (6, 19), 926, and published data from Sites 1267 (24), 1088 (13, 25), 1090 (13), 929 (26). A vertical band highlights the MPT-AMOC-disruption. The horizontal yellow shaded band represents present-day NADW (27). (B) MPT-AMOC-disruption zoom-in. Gray bands highlight the glacial maxima. All the transect Sites show more positive εNd between MIS-25 and 21, thus confirming the MPT-AMOC-disruption is observed basin-wide. The εNd of the MIS-26 glacial maximum is more negative than adjacent interglacial maxima at MIS-25 and MIS-27, uniquely in the record, foreshadowing a negative εNd-excursion, and together reflecting a MIS-27-25 cratonic erosional event that directly preceded the MPT-AMOC-disruption (bright green vertical band).

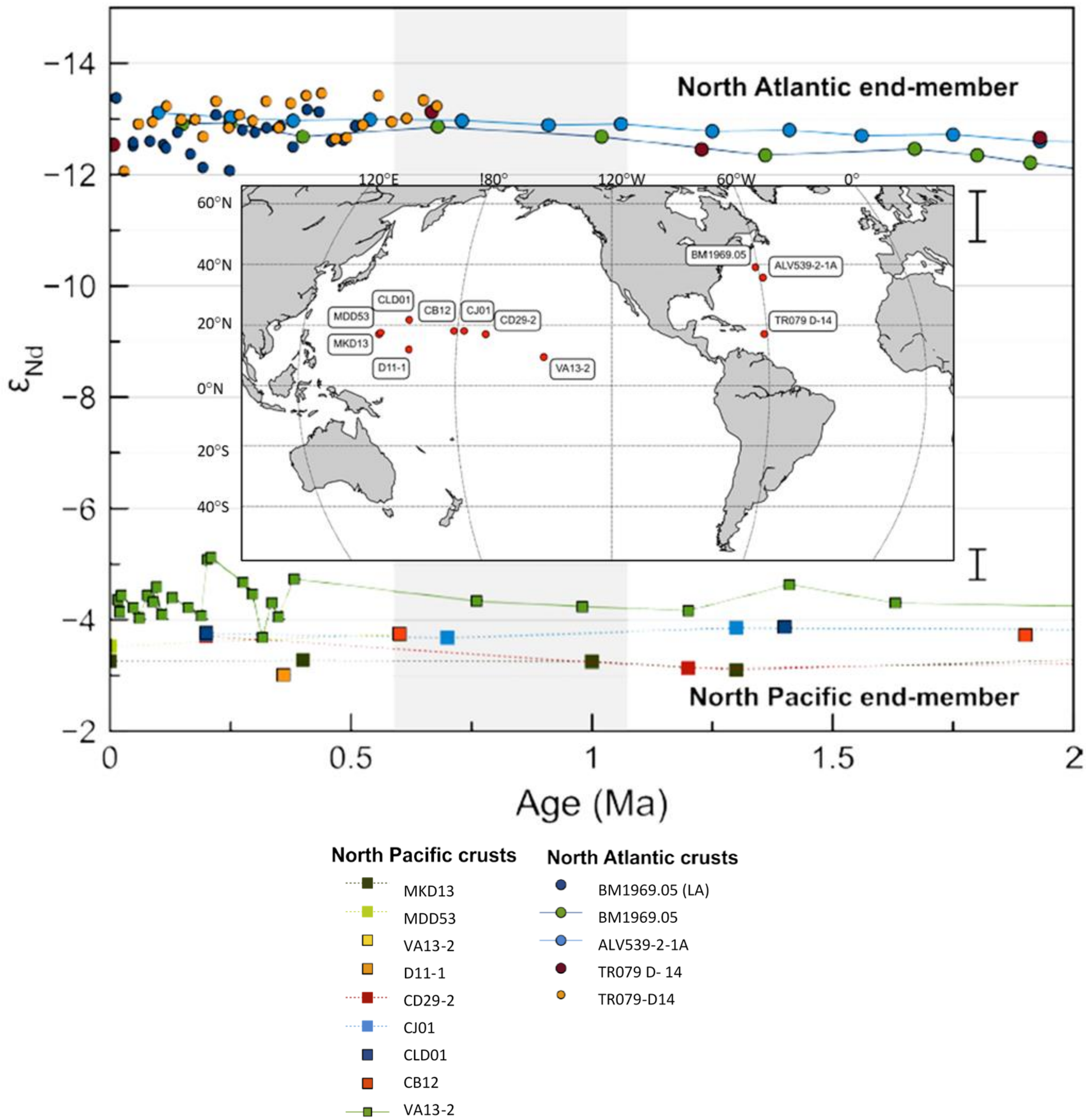

Figure S3*. North Atlantic and North Pacific water-mass end-member εNd-values through time,* from Fe-Mn crust data, sustaining distinctive values of ~ -13 vs. ~-4 through the entire time interval. The low temporal resolution of the Fe-Mn crust data do not show short term changes but highlight the longer term constancy of both end-members over the last 2 Ma. Data site locations red symbols in the map. Figure is modified after Pena and Goldstein (13). See also Figure S8.

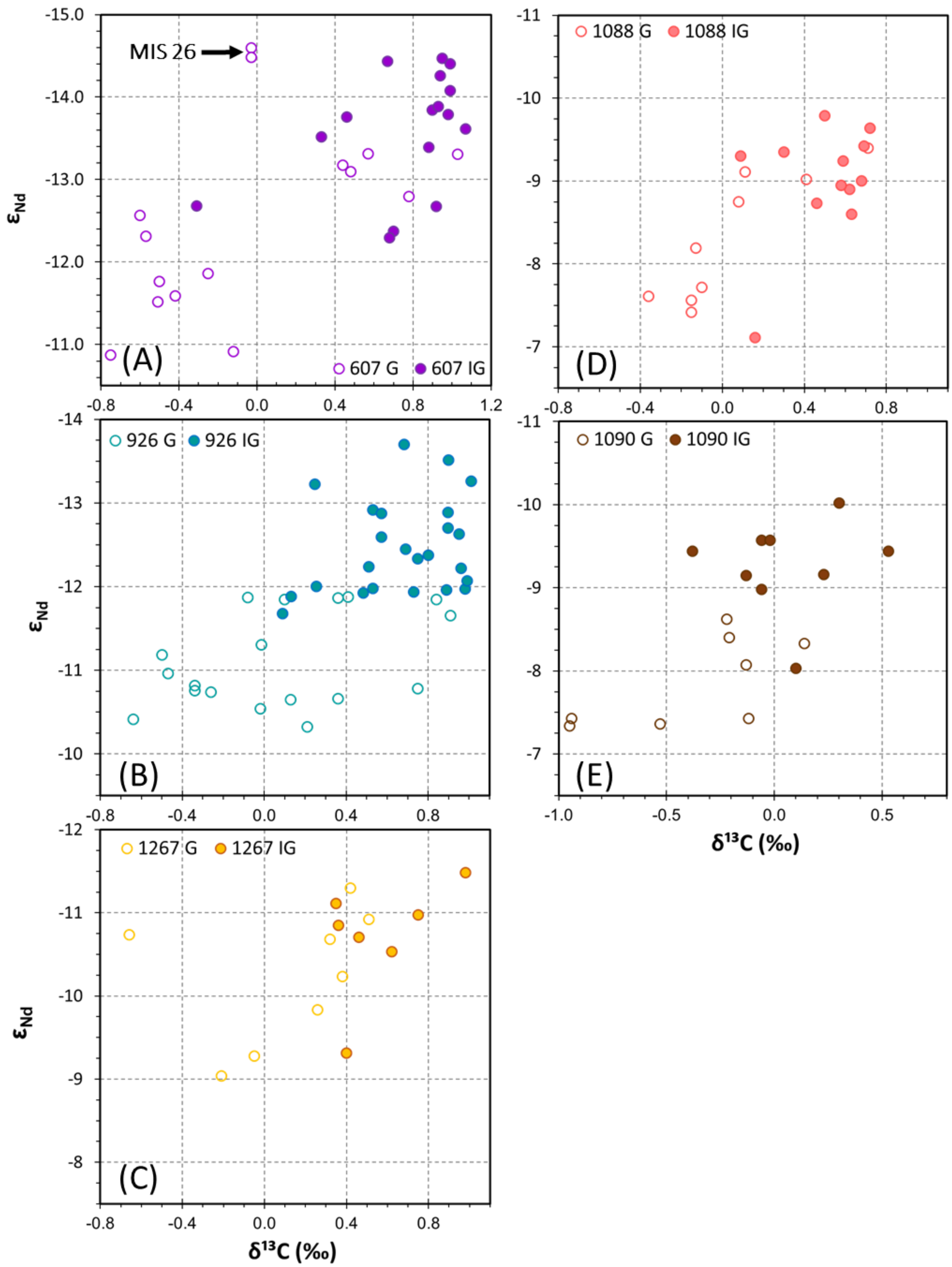

Figure S4. ***εNd vs benthic foraminiferal δ13C during interglacial and glacial maxima for the Sites 607 (A), 926 (B), 1267 (C), 1088 (D) and 1090 (E).*** The anti-correlation is consistent with greater NSW contributions during interglacials (full circles) and SSW incursion during glacials (empty circles).

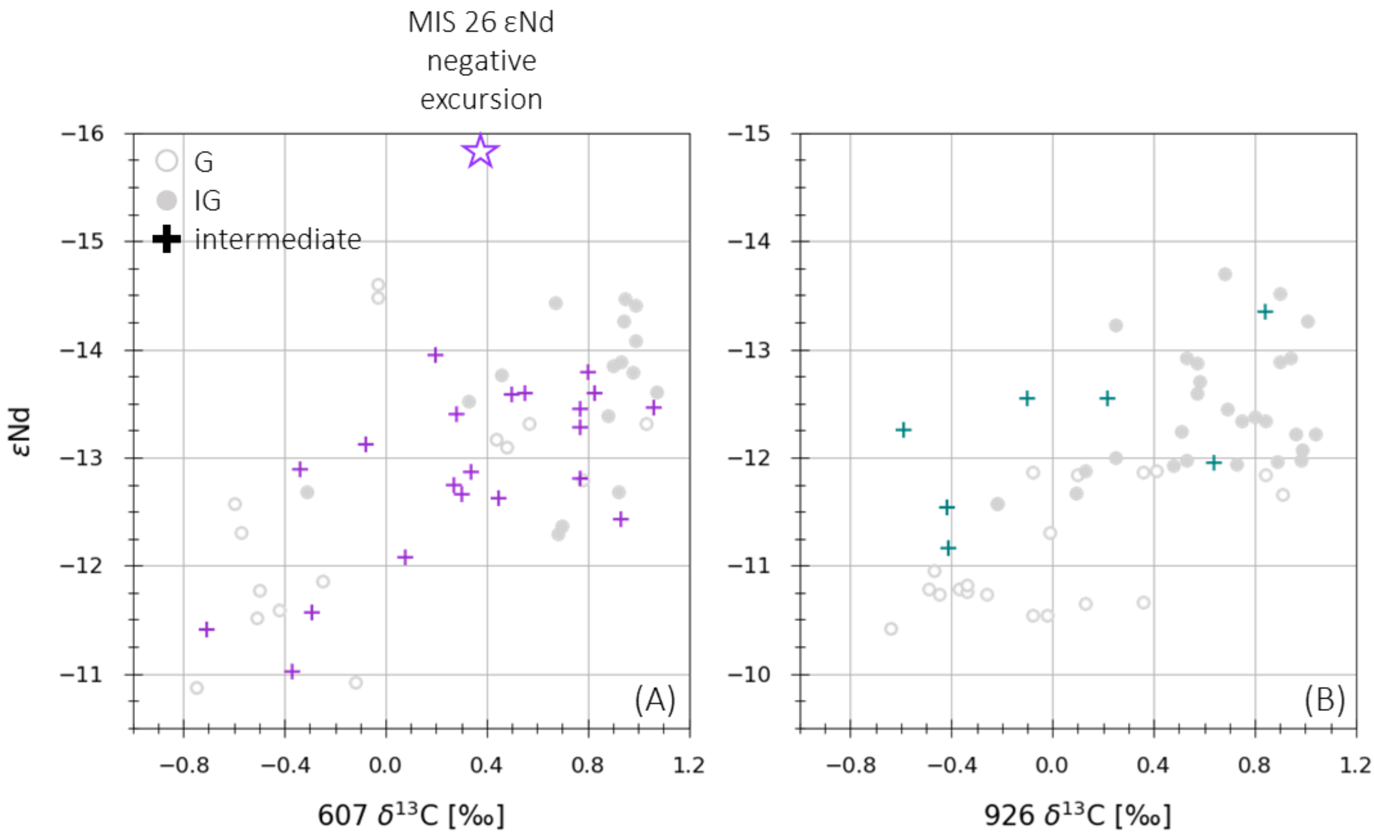

Figure S5. *εNd vs benthic foraminiferal δ13C in between the glacial and interglacial maxima for Sites 607 (a) and 926 (b).* The intermediate points are marked with plus signs in purple (607) and blue (926). The glacial (G, empty circles) and interglacial (IG, full circles) maxima data for each site are marked in gray in the background. The open star sign marks a highly negative intermediate point during MIS-26.

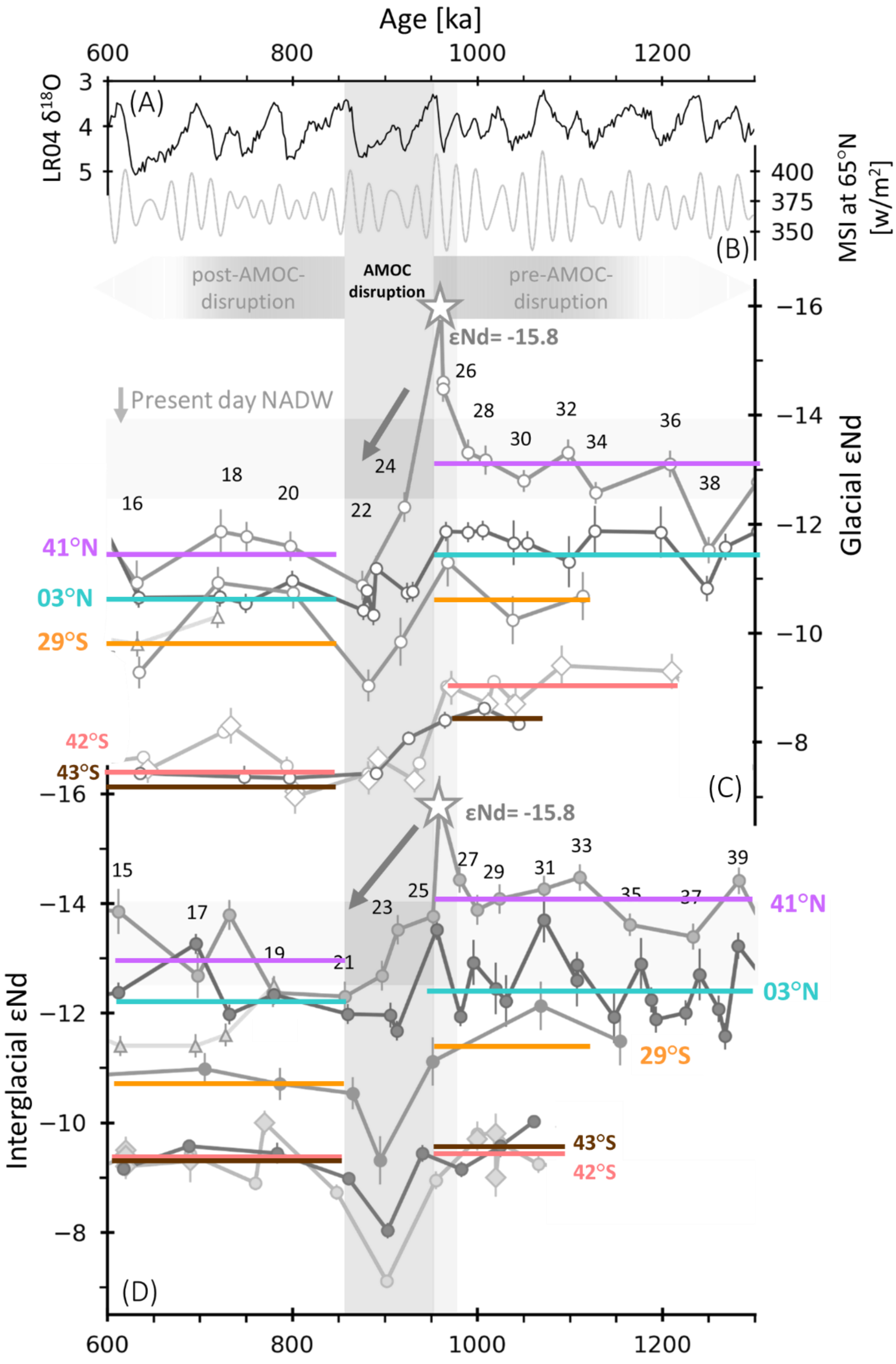

Figure S6: ***Average of (C) glacial and (D) interglacial εNd values at the different sites of the εNd transect***, pre- and post-MPT-AMOC-disruption. The panel assignments are as in Fig. 1 in the main text. Site colors are as in Fig. 1 and Fig. S2.

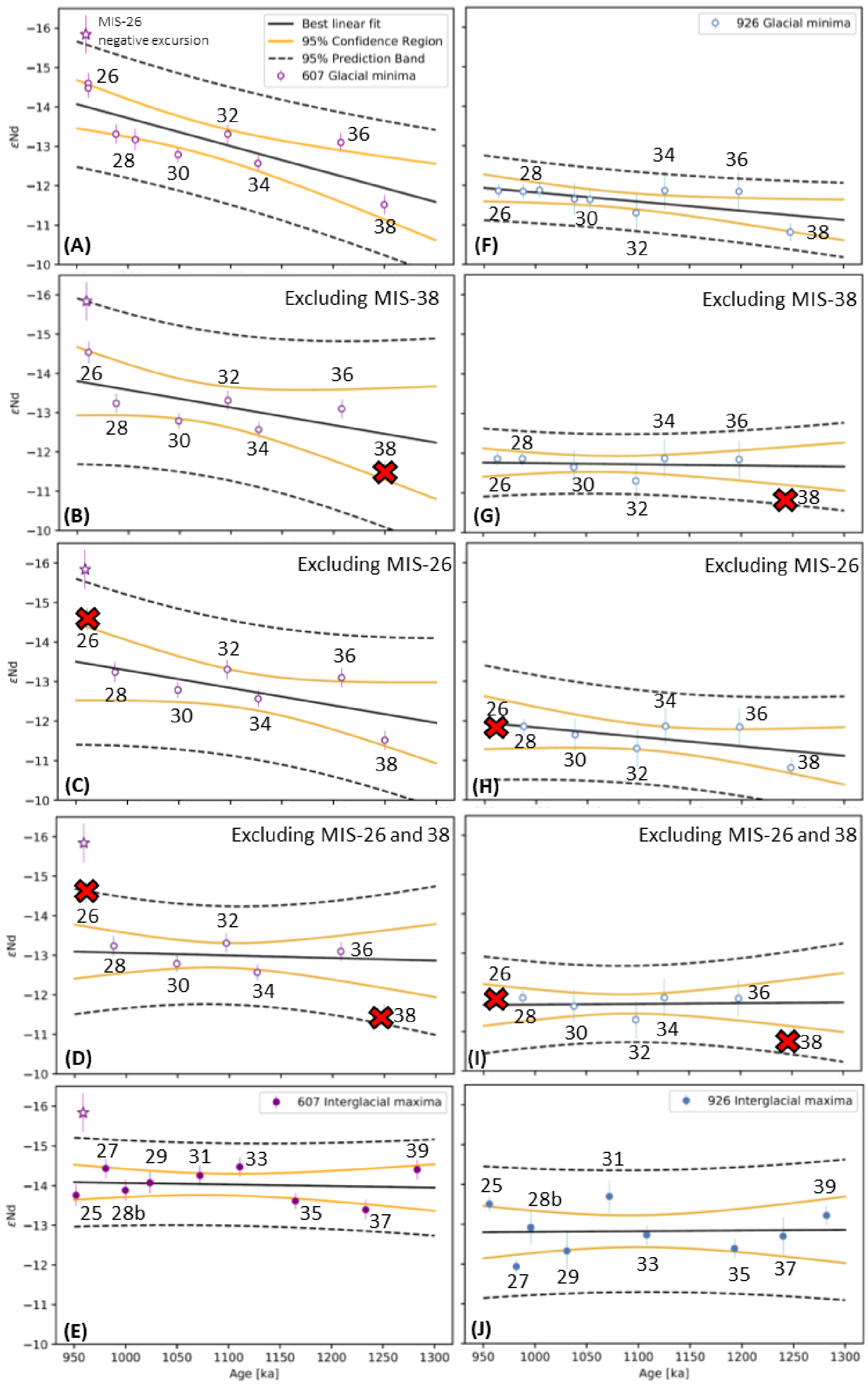
MIS-26
negative excursion
Best linear fit
95% Confidence Region
95% Prediction Band
607 Glacial minima
926 Glacial minima
Excluding MIS-38
Excluding MIS-26
Excluding MIS-26 and 38
607 Interglacial maxima
926 Interglacial maxima
εNd
Age [ka]
(A)
(B)
(C)
(D)
(E)
(F)
(G)
(H)
(I)
(J)

Figure S7. ***Linear regression analyses for pre-MPT-AMOC-disruption period datapoints (MIS-39 to MIS-25), at North and equatorial Atlantic Sites 607 and 926, respectively.*** All points except the star are glacial or interglacial maxima, the star is the highly negative intermediate point in MIS-26. (A) Glacials for all data and (B) excluding MIS-38, (C) glacials excluding MIS-26 (D) glacials excluding both MIS-38 and MIS-26. (A-D) also show the MIS 26 intermediate point (star) showing a negative εNd excursion, from Site 607. (E) Interglacial data from Site 607. The optimal regression values are presented in Table S5. In (B) and (C), while the slope of the linear regression is lower than in (A), it remains positive (Table S5). (F,G,H, I) Glacial and (J) interglacial maxima analyses for Site 926. The analysis included constructing a linear regression model for each data set and determination of the 95% confidence interval and 95% prediction band for each regression. In all cases the MIS-26 negative εNd excursion is outside the bounds of both glacial and interglacial 95% prediction bands.

Figure S8. ***Ice rafted debris (IRD)*** observed in the MIS-26 intermediate sample showing the negative εNd excursion at North Atlantic Site 607 (from 19).

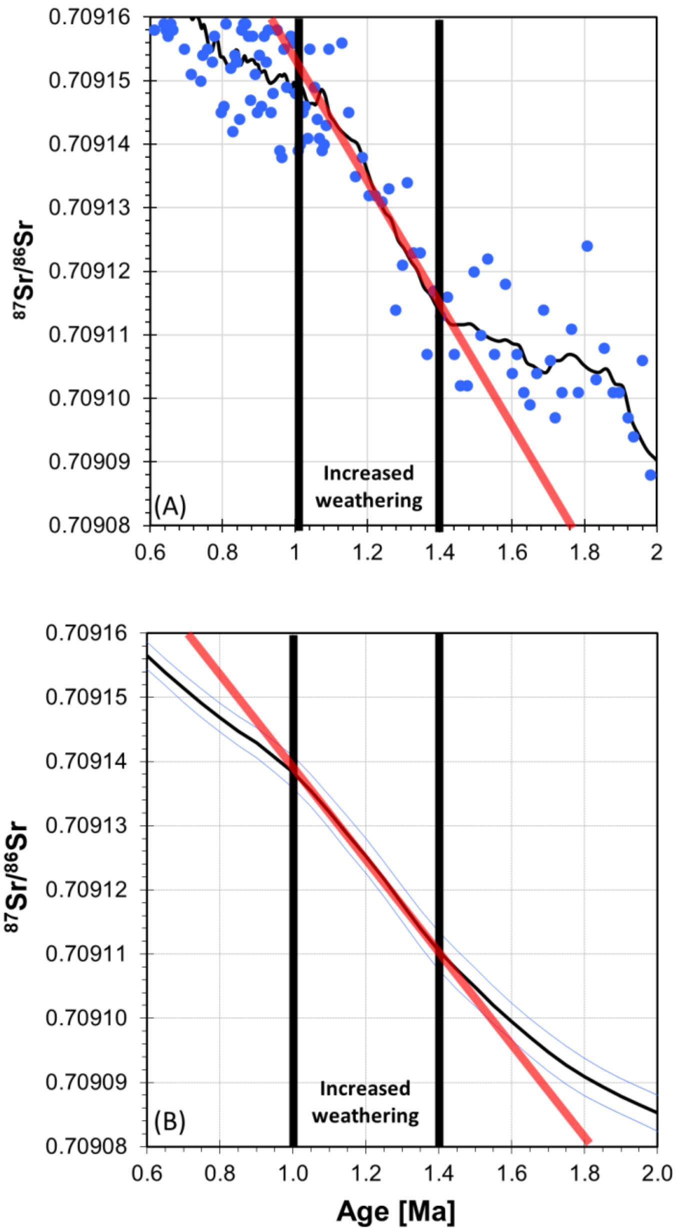

Figure S9: ***The seawater Sr-isotope curve 2.0-0.6 Ma.*** (A) The early-mid-Pleistocene data from Farrell et al. (28) are plotted, the black line going through the data is based on a running average of ~100 kyr, depending on the data density. These data are used in the main text in Figures 4 and 6. (B) The same time interval is shown with LOWESS fit of the global synthesis version V4B 08 04 of McArthur and Howarth (29), courtesy of J. McArthur. The thin black line shows the best estimate of the curve and the light blue lines show the 95% confidence limits. In both frames, the thick black vertical black lines demark 1.4 and 1.0 Ma. The red lines show that the slope of the 1.4-1.0 Ma time interval is steeper than before or afterward, which we interpret as evidence of increased continental weathering approaching the MPT shift in interglacial-glacial cyclicity; Figure 3 (main text) shows that source is weathering of the Northern Hemisphere continents into the North Atlantic. Frame A clearly shows that the data density is lower between 1.5-1.1 Ma compared to before and after, and a large range of values at ~ 1 Ma, which obscures the timing of the slope shifts. Using the LOWESS fit the shifts are at 1.4 and 1.0 Ma. The long residence time of marine Sr, the large range of values at 1.0 Ma, and the low data density over the 1.4-1.0 Ma time intervals make the precise timing of the shift unclear.

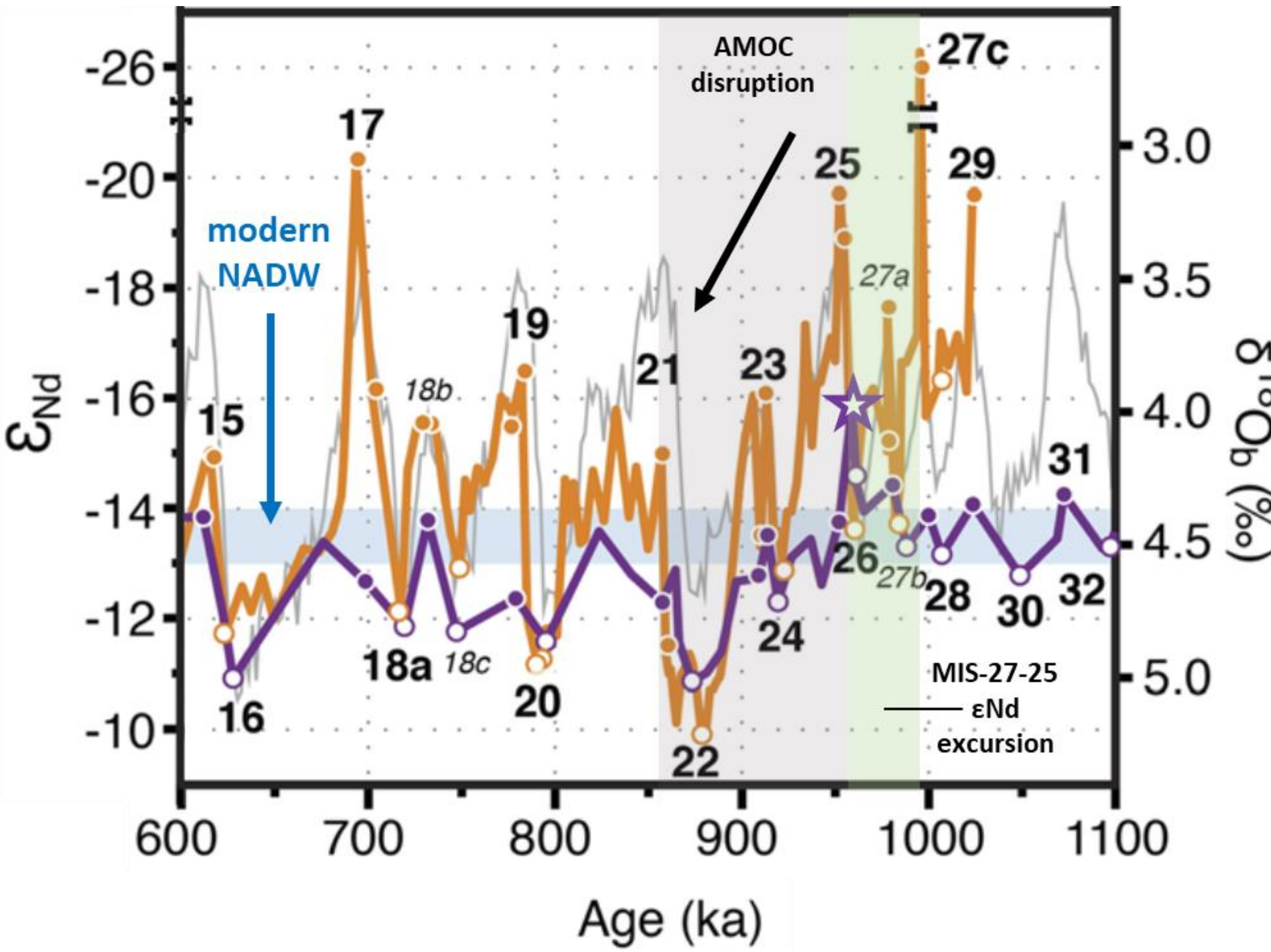

Figure S10: *Comparison between data from Site 607 (purple) and Site 1063 (orange)* modified after ref. **18.** Glacial (open circles) and interglacial (closed circles) εNd maxima were chosen following the glacial-interglacial maxima defined by the LR04 stack (gray line; 23). Interglacial maxima are filled circles and glacial maxima are empty circles. The star represents the very negative value at Site 607 during MIS-26. The vertical shaded gray band shows the timing of the MPT-AMOC-disruption and the shaded green band shows the MIS-27-25 εNd excursion. The horizontal blue band represents εNd value of the present day NADW. Site 1063 εNd values prior to the MPT-AMOC-disruption are showing a greater sensitivity to cratonic shield input (which is expressed by very negative values between MIS-29 and MIS-25), compared to the εNd values after MIS-25. After the MPT-AMOC-disruption, the glacial values of the North Atlantic are overwhelmed by SSW and this is confirmed by the observation that during glacial maxima, the εNd-values of Site 1063 and Site 607 generally match each other, in contrast to interglacials (see also, Fig. 5 in the main text).

Supplementary Tables 1–3 captions: Neodymium isotope data for samples from DSDP Site 607, ODP Site 926 and ODP Site 1267. Depth (meters composite depth) and their ages for DSDP Site 607 are from (6). Depth (meters composite depth) for ODP Site 926 is from (21) and ages are newly tied to LR04 stack (Table S4). Depth (meter composite depth) and ages are from (20). Marine Isotope Stages (MIS) for each interval are listed and assigned according to (23, 30). Samples were chosen to represent the glacial and interglacial maxima with some transitional points (marked with / in the MIS column). Values plotted in Figure S7 are marked with * in the MIS column. The in-run errors (2σ) and external reproducibility errors are listed in the table.

Table S1. DSDP Site 607 (41°00'N, 32°58'W, 3427 m). The data were generated by Joohee Kim and are from Kim et al. (6, 19), deposited in EarthChem.

DSDP Site 607 Nd isotope ratios							
Depth (mcd)	**Age (ka)**	**$^{143}Nd/^{144}Nd$**	**± 2σ in-run**	**εNd**	**± 2σ in-run**	**± 2σ ext.**	**MIS**
21.45	573	0.511976	10	-12.91	0.19	0.29	15a
22.05	596	0.511928	21	-13.84	0.42	0.29	15b
23.23	612	0.511928	36	-13.85	0.70	0.41	15e
24.43	622	0.512019	09	-12.08	0.17	0.24	15e/16a
24.88	628	0.512078	15	-10.92	0.29	0.41	16a
27.30	676	0.511951	12	-13.40	0.23	0.24	16c
28.33	699	0.511988	16	-12.68	0.32	0.41	17
29.23	719	0.512030	14	-11.86	0.28	0.41	18a
29.83	732	0.511931	09	-13.79	0.11	0.27	18b
30.58	747	0.512035	06	-11.77	0.14	0.27	18e
31.72	779	0.512004	10	-12.37	0.09	0.27	19
32.32	795	0.512044	06	-11.59	0.10	0.27	20
33.07	813	0.511979	12	-12.86	0.23	0.24	20/21
33.39	824	0.511941	13	-13.59	0.25	0.24	20/21
33.82	841	0.511982	11	-12.81	0.22	0.24	20/21
34.27	858	0.512008	06	-12.30	0.10	0.27	21
34.49	864	0.511977	13	-12.89	0.25	0.24	21/22
34.57	866	0.512045	12	-11.57	0.24	0.24	21/22
34.87	873	0.512081	05	-10.87	0.20	0.27	22
35.17	881	0.512073	12	-11.02	0.24	0.24	22/23b
35.47	889	0.512053	11	-11.41	0.22	0.24	22/23b
35.77	897	0.511988	07	-12.68	0.11	0.27	23b
36.39	909	0.511985	09	-12.74	0.18	0.24	23b/23c
36.67	914	0.511945	09	-13.52	0.12	0.27	23c
36.97	919	0.512007	05	-12.31	0.18	0.27	24
37.33	927	0.511965	12	-13.12	0.24	0.24	24/25
37.74	937	0.511949	12	-13.45	0.24	0.24	24/25
38.02	943	0.511991	13	-12.62	0.25	0.49	24/25
38.49	952	0.511933	08	-13.76	0.17	0.27	25
38.75	959	0.511826	18	-15.84	0.36	0.49	~26*

38.83	961	0.511890	05	-14.60	0.20	0.27	26*
38.83	961	0.511896	17	-14.48	0.33	0.24	26*
38.99	965	0.511923	12	-13.95	0.24	0.24	~26
39.65	981	0.511898	12	-14.43	0.24	0.24	27*
39.97	988	0.511956	12	-13.31	0.23	0.24	28a*
40.57	1000	0.511926	11	-13.88	0.19	0.27	28b*
40.84	1007	0.511963	05	-13.17	0.16	0.27	28c*
41.62	1024	0.511916	10	-14.08	0.21	0.27	29*
42.87	1049	0.511982	06	-12.79	0.16	0.20	30*
43.79	1069	0.511948	10	-13.46	0.10	0.20	~31
43.92	1072	0.511907	11	-14.26	0.22	0.24	31*
44.67	1093	0.511957	14	-13.28	0.27	0.27	~32
44.82	1097	0.511956	12	-13.31	0.24	0.24	32*
44.90	1100	0.511942	11	-13.58	0.22	0.27	~32
45.04	1104	0.512001	08	-12.43	0.16	0.27	~33
45.40	1111	0.511896	11	-14.47	0.22	0.24	33*
45.57	1114	0.511931	11	-13.79	0.21	0.27	~33
46.02	1127	0.511994	05	-12.57	0.10	0.20	34*
47.30	1165	0.511940	08	-13.61	0.11	0.20	35*
49.39	1208	0.511967	12	-13.10	0.23	0.24	36*
49.92	1224	0.511941	10	-13.60	0.19	0.27	36/37
50.22	1233	0.511951	10	-13.39	0.20	0.24	37*
51.04	1250	0.512048	12	-11.52	0.23	0.24	38*
51.29	1254	0.511989	09	-12.66	0.17	0.27	~38
53.37	1283	0.511899	10	-14.41	0.19	0.24	39*

Table S2. ODP 926 (3°43'N, 42°55'W, 3599 m). The data were generated by Maayan Yehudai and are from Yehudai et al. (21), deposited in EarthChem.

ODP Site 926 Nd isotope ratios							
Depth (mcd)	**Age (ka)**	^{143}**Nd/**^{144}**Nd**	**± 2σ in-run**	**εNd**	**± 2σ in-run**	**± 2σ ext.**	**MIS**
20.92	575	0.511991	09	-12.63	0.18	0.18	15a
21.02	585	0.512012	15	-12.21	0.28	0.18	15b
21.92	612	0.512004	08	-12.37	0.16	0.18	15e
22.22	630	0.512092	07	-10.65	0.13	0.18	16a
24.12	696	0.511958	10	-13.26	0.19	0.18	17c
24.92	718	0.512091	09	-10.66	0.17	0.18	18a
25.22	732	0.512098	10	-11.98	0.19	0.18	18b
25.82	746	0.512098	10	-10.54	0.19	0.18	18e
26.82	780	0.512006	17	-12.34	0.33	0.18	19c
27.17	797	0.512076	10	-10.96	0.20	0.18	20a
29.08	860	0.512024	10	-11.98	0.20	0.18	21g
29.18	864	0.512066	07	-11.16	0.15	0.18	21/22
29.38	874	0.512104	10	-10.42	0.19	0.18	22
29.48	877	0.512085	07	-10.78	0.13	0.23	22
29.68	885	0.512109	10	-10.33	0.19	0.18	23a
29.78	888	0.512065	07	-11.18	0.14	0.23	23a
30.27	906	0.512025	09	-11.96	0.17	0.23	23c
30.48	913	0.512039	09	-11.68	0.18	0.18	23c
30.58	916	0.512010	11	-12.25	0.21	0.27	24/23c
30.78	922	0.512087	14	-10.74	0.27	0.18	24
30.98	928	0.512086	09	-10.76	0.17	0.18	24
31.18	935	0.511910	15	-11.54	0.29	0.47	24/25
31.44	943	0.511995	14	-12.55	0.28	0.49	24/25
31.86	956	0.511945	11	-13.51	0.22	0.18	25e*
32.14	964	0.512030	20	-11.86	0.40	0.18	26*
32.66	982	0.512026	10	-11.94	0.20	0.18	27*
32.84	988	0.512031	11	-11.85	0.21	0.18	28a*
33.14	996	0.511976	36	-12.92	0.71	0.41	28b*
33.24	1004	0.512029	07	-11.88	0.14	0.18	28c*
33.54	1020	0.511864	13	-12.45	0.26	0.47	29a*
33.94	1031	0.511876	20	-12.22	0.39	0.47	29*
34.04	1034	0.511954	12	-13.35	0.24	0.16	29/30
34.16	1038	0.512041	10	-11.65	0.19	0.41	30*
34.44	1053	0.512041	10	-11.64	0.19	0.23	30b
34.74	1068	0.512025	18	-11.95	0.35	0.18	31/30
34.81	1072	0.511936	10	-13.70	0.20	0.41	31*
35.61	1098	0.511922	44	-11.31	0.86	0.47	32*

35.81	1108	0.511857	20	-12.59	0.40	0.47	33*
35.81	1108	0.511978	13	-12.87	0.26	0.24	33*
36.11	1126	0.511894	20	-11.87	0.40	0.47	34*
36.91	1148	0.511891	19	-11.92	0.37	0.47	~35
37.71	1177	0.511841	12	-12.89	0.22	0.47	~35
37.91	1188	0.512011	07	-12.24	0.13	0.23	35*
38.01	1193	0.512029	10	-11.88	0.19	0.24	35*
38.11	1198	0.511895	18	-11.85	0.35	0.47	36*
38.81	1225	0.512023	08	-12.00	0.16	0.23	37
38.91	1240	0.511851	18	-12.70	0.35	0.47	37*
39.51	1248	0.512083	10	-10.82	0.19	0.23	38*
40.21	1261	0.512019	16	-12.07	0.31	0.24	~39
40.61	1268	0.512045	12	-11.58	0.23	0.24	~39
41.41	1282	0.511960	12	-13.22	0.24	0.24	39*

Table S3.: ODP Site 1267 (28°6´S, 1°43´E, 4355 m). ODP 1267 data are published in Farmer et al. (24).

ODP Site 1267 Nd isotope ratios							
Depth (mcd)	**Age (ka)**	**$^{143}Nd/^{144}Nd$**	**± 2σ in-run**	**εNd**	**± 2σ in-run**	**± 2σ ext.**	**MIS**
5.75	573	0.512082	10	-10.85	0.16	0.29	15
6.20	631	0.512162	08	-9.28	0.14	0.29	16
6.74	705	0.512075	07	-10.98	0.12	0.29	17
6.82	716	0.512078	07	-10.92	0.12	0.29	18
7.17	787	0.512089	09	-10.70	0.15	0.29	19
7.22	798	0.512088	08	-10.74	0.13	0.29	20
7.34	866	0.512098	07	-10.53	0.12	0.29	21
7.49	880	0.512175	07	-9.04	0.12	0.29	22
7.64	895	0.512161	11	-9.31	0.13	0.44	23
7.84	915	0.512134	08	-9.84	0.09	0.44	24
8.19	952	0.512068	11	-11.12	0.12	0.44	25
8.34	966	0.512059	07	-11.30	0.08	0.44	26
9.09	1037	0.512113	08	-10.24	0.09	0.44	30
9.42	1069	0.512016	11	-12.13	0.12	0.44	31
10.02	1113	0.512090	11	-10.68	0.12	0.44	34
10.49	1155	0.512049	11	-11.48	0.13	0.44	35

Table S4. Tie-points between LR04 benthic δ18O stack ages (23) and Site 926 δ18O depths (20), used for age-model production for Site 926 which was not included in the LR04 stack.

LR04 tie-point age (ka)	LR04 tie-point $\delta^{18}O$ (‰)	926 tie point depth (mcd)	926 $\delta^{18}O$ (‰)	MIS
2	3.2	0.11	3.1	1
18	5.0	0.51	4.9	2
38	4.4	1.51	4.2	tr
123	3.1	4.79	2.9	5
140	5.0	5.39	4.8	6
192	3.8	7.39	3.7	tr
199	3.6	7.79	3.4	7a
216	3.5	8.59	3.3	7c
239	3.4	9.59	4.0	7e
252	4.6	9.99	4.6	8a
286	3.8	11.36	3.6	9a
329	3.2	12.76	3.0	9e
341	4.8	13.16	4.9	10a
406	3.2	15.62	3.0	11c
434	5.1	16.22	5.2	12a
491	3.5	18.42	3.4	13a
513	4.3	19.02	4.0	13b
524	3.8	19.32	3.7	13c
536	4.6	19.62	4.4	14a
566	3.9	20.42	3.8	tr
575	3.4	20.92	3.3	15a
585	4.3	21.02	4.3	15b
612	3.5	21.92	3.3	15e
630	5.1	22.22	5.0	16a
696	3.5	24.12	3.4	17c
718	4.8	24.92	4.5	18a
732	4.0	25.22	3.8	18b
746	4.7	25.82	4.5	18e
780	3.5	26.82	3.3	19c
794	4.7	27.07	4.6	20a
860	3.5	29.08	2.9	21g
874	4.7	29.38	4.7	22
910	4.0	30.38	3.9	23c
922	4.6	30.78	4.4	24
956	3.3	31.86	3.1	25e
964	4.6	32.14	4.3	26
978	3.7	32.54	3.5	27
988	4.2	32.84	3.9	28a
996	3.8	33.14	3.6	28b
1004	4.3	33.24	4.2	28c
1016	3.7	33.34	3.7	tr
1022	3.6	33.64	3.4	29
1038	4.5	34.16	4.3	30
1072	3.2	34.81	3.3	31
1098	4.3	35.61	4.3	32
1108	3.7	35.81	3.3	33
1126	4.5	36.11	4.3	34
1162	3.6	37.41	3.4	35
1198	4.4	38.11	4.5	36
1240	3.3	39.21	2.9	37
1248	4.4	39.51	4.7	38
1282	3.7	41.41	3.1	39
1288	4.3	41.46	4.2	40
1316	3.6	42.76	2.8	41
1340	4.2	43.06	4.1	42

1352	3.5	43.76	3.2	43
1374	4.2	44.17	4.1	44
1400	3.6	45.26	2.9	45
1412	4.4	45.56	4.4	46
1440	3.3	46.35	2.8	47
1456	4.3	46.95	4.3	48
1474	3.4	47.35	3.2	49
1496	4.4	48.15	4.5	50
1523	3.7	49.35	3.2	51

Table S5. Linear regression parameter results for glacial minima and interglacial maxima from sites 607 and 926, for MISs 39-25.

Dataset	Correlation coefficient (R^2)	Slope (a)	Intercept (b)
607 Glacial maxima (*Fig. 6SA*)	0.64	0.007 ± 0.002	-20.8 ± 2.1
607 Glacial maxima (No MIS-38, *Fig. 6SB*)	0.35	0.005 ± 0.003	-18.1 ± 3.2
607 Glacial maxima (No MIS-26 *Fig. 6SC*)	0.42	0.004 ± 0.003	-17.7 ± 2.9
607 Glacial maxima (No MIS-38,26, *Fig. 6SD*)	0.03	0.0007 ± 0.0022	-13.7 ± 2.4
607 Interglacial maxima (*Fig. 6SE*)	0.01	0.0004 ± 0.0013	-14.5 ± 1.4
926 Glacial maxima (*Fig. 6SF*)	0.39	0.002 ± 0.001	-14.1 ± 1.2
926 Glacial maxima (No MIS-38, *Fig. 6SG*)	0.01	0.0003 ± 0.0013	-12.1 ± 1.4
926 Glacial maxima (No MIS-26, *Fig. 6SH*)	0.30	0.002 ± 0.002	-14.2 ± 2.0
926 Glacial maxima (No MIS-38,26, *Fig. 6SI*)	0.004	-0.0002 ± 0.0017	-11.5 ± 1.9
926 Interglacial maxima (*Fig. 6SJ*)	0.001	-0.0002 ± 0.0018	-12.6 ± 2.0

Table S6. Statistical analysis results for εNd variability during pre and post AMOC disruption.

IG-G* pre-AMOC-disruption variability				
Parameter	**Site**	**Average**	**Median**	**2sd****
MIS-39 to MIS-25	607	-13.62	-13.69	1.63
	926	-12.21	-11.97	1.36
	1267	-11.16	-11.21	1.31
	1088	-9.21	-9.11	0.77
	1090	-9.08	-9.15	1.29
IG pre- AMOC-disruption variability				
MIS-39 to MIS-25	607	-14.03	-14.08	0.78
	926	-12.77	-12.87	1.31
	1267	-11.58	-11.48	1.03
	1088	-9.45	-9.64	0.75
	1090	-9.55	-9.51	0.72
G pre- AMOC-disruption variability				
MIS-38 to MIS-26	607	-13.21	-13.17	1.87
	926	-11.64	-11.85	0.72
	1267	-10.74	-10.51	0.00005
	1088	-9.00	-9.01	0.54
	1090	-8.45	-8.40	0.30
IG-G post- AMOC-disruption variability				
MIS-21 to MIS-15	607	-12.34	-12.30	1.95
	926	-11.64	-11.98	1.93
	1267	-10.57	-10.74	1.18
	1088	-8.57	-8.82	1.91
	1090	-8.47	-8.98	2.08
IG post- AMOC-disruption variability				
MIS-21 to MIS-15	607	-13.00	-12.68	1.53
	926	-12.38	-12.34	1.05
	1267	-10.77	-10.78	0.38
	1088	-9.31	-9.35	0.72
	1090	-9.29	-9.30	0.53
G post- AMOC-disruption variability				
MIS-20 to MIS-16	607	-11.53	-11.68	0.85
	926	-10.70	-10.66	0.36
	1267	-10.31	-10.74	1.80
	1088	-7.62	-7.56	0.99
	1090	-7.38	-7.36	0.09

* IG=Interglacial, G=Glacial
** sd=standard deviation

Supplementary Information References

1. S. L. Goldstein, S. R. Hemming, Long-lived Isotopic Tracers in Oceanography, Paleoceanography, and Ice-sheet Dynamics. *Treatise Geochemistry Second Ed.* **8**, 453–489 (2003).
2. M. Frank, Radiogenic isotopes: Tracers of past ocean circulation and erosional input. *Rev. Geophys.* **40**, 1–38 (2002).
3. T. van de Flierdt, *et al.*, Neodymium in the oceans: a global database, a regional comparison and implications for palaeoceanographic research. *Philos. Trans. R. Soc. A Math. Phys. Eng. Sci.* **374**, 20150293 (2016).
4. F. Lacan, K. Tachikawa, C. Jeandel, Neodymium isotopic composition of the oceans: A compilation of seawater data. *Chem. Geol.* **300–301**, 177–184 (2012).
5. S. L. Bates, M. Siddall, C. Waelbroeck, Hydrographic variations in deep ocean temperature over the mid-Pleistocene transition. *Quat. Sci. Rev.* **88**, 147–158 (2014).
6. J. Kim, *et al.*, Nd isotope ratios from DSDP Site 607 in the deep North Atlantic over the last 1.5 Myr. *Interdiscip. Earth Data Alliance* (2020) https:/doi.org/10.26022/IEDA/111576. Deposited: 2020-08-31.
7. J. Yu, S. Broecker, Wallace, Comment on "Pliocene-Pleistocene Climate Transitions ". *Science* **328**, 1480 (2010).
8. H. J. Spero, J. Bijma, D. W. Lea, B. E. Bemis, Effect of seawater carbonate concentration on foraminiferal carbon and oxygen isotopes. *Nature* **390**, 497–500 (1997).
9. H. Elderfield, Foraminifera Mg/Ca paleothermometry: expected advances and unexpected consequences. *Geochim. Cosmochim. Acta* **66**, A213 (2002).
10. R. L. Rutberg, S. R. Hemming, S. L. Goldstein, Reduced North Atlantic Deep Water flux to the glacial Southern Ocean inferred from neodymium isotope ratios. *Nature* **405**, 935–938 (2000).
11. A. M. Piotrowski, S. L. Goldstein, S. R. Hemming, R. G. Fairbanks, Temporal relationships of carbon cycling and ocean circulation at glacial boundaries. *Science* **307**, 1933–1938 (2005).
12. N. L. Roberts, A. M. Piotrowski, J. F. McManus, L. D. Keigwin, Synchronous Deglacial Overturning and Water Mass Source Changes. *Science* **327**, 75–78 (2010).
13. L. D. Pena, S. L. Goldstein, Thermohaline circulation crisis and impacts during the mid-Pleistocene transition. *Science* **345**, 318–322 (2014).
14. M. Gutjahr, M. Frank, C. H. Stirling, L. D. Keigwin, A. N. Halliday, Tracing the Nd isotope evolution of North Atlantic Deep and Intermediate Waters in the western North Atlantic since the Last Glacial Maximum from Blake Ridge sediments. *Earth Planet. Sci. Lett.* (2008) https:/doi.org/10.1016/j.epsl.2007.10.037.
15. A. N. Abbott, B. A. Haley, J. McManus, The impact of sedimentary coatings on the diagenetic Nd flux. *Earth Planet. Sci. Lett.* **449**, 217–227 (2016).
16. J. Du, B. A. Haley, A. C. Mix, M. H. Walczak, S. K. Praetorius, Flushing of the deep Pacific Ocean and the deglacial rise of atmospheric CO2 concentrations. *Nat. Geosci.* **11**, 749–755 (2018).
17. F. Lacan, C. Jeandel, Neodymium isotopes as a new tool for quantifying exchange fluxes

at the continent-ocean interface. *Earth Planet. Sci. Lett.* **232**, 245–257 (2005).

18. M. Jaume-Seguí, *et al.*, Distinguishing Glacial AMOC and Interglacial Non-AMOC Nd Isotopic Signals in the Deep Western Atlantic Over the Last 1 Myr. *Paleoceanogr. Paleoclimatology* **36**, 1–21 (2021).
19. J. Kim, *et al.*, North Atlantic Deep Water during Pleistocene interglacials and glacials. *Quat. Sci. Rev.* **269**, 107146 (2021).
20. T. Bickert, W. Curry, G. Wefer, Late Pliocene to Holocene (2.6-0 Ma) western equatorial Atlantic deep-water circulation: Inferences from benthic stable isotopes. *Proc. Ocean Drill. Program, Sci. Results* **154**, 239–254 (1997).
21. M. Yehudai, *et al.*, Nd isotope ratios from ODP Leg 154, Site 926 in the deep Equatorial Atlantic over the last 1.5 Myr. *Interdiscip. Earth Data Alliance* (2020) https:/doi.org/10.26022/IEDA/111588. Deposited: 2020-09-30.
22. M. E. Raymo, W. F. Ruddiman, N. J. Shackleton, D. W. Oppo, Evolution of Atlantic-Pacific δ13C gradients over the last 2.5 m.y. *Earth Planet. Sci. Lett.* **97**, 353–368 (1990).
23. L. E. Lisiecki, M. E. Raymo, A Pliocene-Pleistocene stack of 57 globally distributed benthic d18O records. *Paleoceanography* **20**, 1–17 (2005).
24. J. R. Farmer, *et al.*, Deep Atlantic Ocean carbon storage and the rise of 100,000-year glacial cycles. *Nat. Geosci.* **12**, 355–360 (2019).
25. V. Dausmann, M. Frank, M. Gutjahr, J. Rickli, Glacial reduction of AMOC strength and long-term transition in weathering inputs into the Southern Ocean since the mid-Miocene: Evidence from radiogenic Nd and Hf isotopes. *Paleoceanography* **32**, 1–19 (2017).
26. J. N. W. Howe, A. M. Piotrowski, Atlantic deep water provenance decoupled from atmospheric CO2 concentration during the lukewarm interglacials. *Nat. Commun.* **8**, 1–7 (2017).
27. M. Lambelet, *et al.*, Neodymium isotopic composition and concentration in the western North Atlantic Ocean : Results from the GEOTRACES GA02 section. *Geochim. Cosmochim. Acta* **177**, 1–29 (2016).
28. J. W. Farrell, S. C. Clemens, L. P. Gromet, Improved chronostratigraphic reference curve of late Neogene seawater 87 Sr/ 86 Sr. *Geology* **23**, 403–406 (1995).
29. J. McArthur, R. J. Howarth, “Strontium isotope stratigraphy” in *A Geologic Time Scale 2004*, (2005), p. 589 pp.
30. L. B. Railsback, P. L. Gibbard, M. J. Head, N. R. G. Voarintsoa, S. Toucanne, An optimized scheme of lettered marine isotope substages for the last 1.0 million years, and the climatostratigraphic nature of isotope stages and substages. *Quat. Sci. Rev.* **111**, 94–106 (2015).